Multiscale Richtmyer-Meshkov instability experiments to isolate the strain rate dependence of strength

Michael B. Prime ●,* Saryu J. Fensin ●, David R. Jones ●, Joshua W. Dyer ●, and Daniel T. Martinez ●

Los Alamos National Laboratory (LANL), Los Alamos, New Mexico 87545, USA

Theoretical analysis of Richtmyer-Meshkov instability (RMI) experiments for solid strength shows that the strain rate for a given shock should be inversely proportional to the length scale of the sine wave perturbations when $\eta_0 k$, the nondimensional amplitude to wavelength ratio, is held fixed. To isolate the effect of strain rate on strength, free-surface RMI specimens of annealed copper were prepared with three perturbation regions with the same $\eta_0 k$ but different length scales, characterized by the wavelength λ varying by a factor of 4.9 from 65 to 130 to 320 μm. Three such targets with different fixed $\eta_0 k's$ were impacted to a shock pressure of 25 GPa, and the instability evolution was measured with photon Doppler velocimetry. Strengths estimated by comparing hydrocode simulation to the data increased from 700 to 1200 MPa as λ decreased. The different $\eta_0 k$ targets exercised increasing amounts of plastic strain yet showed no evidence of strain hardening. Physical regime sensitivity analysis determined that for $320 - 65$ μm wavelength perturbations, the effective strain rates increased from 8.7×10^6 to 3.3×10^7 s^{-1}, a factor of 3.8. Thus, the predicted strain rate scaling was mostly achieved but slightly suppressed by increased strength at higher rates. The RMI strength estimates were plotted against constitutive testing data on copper from the literature to show striking evidence of the strength upturn at higher strain rates.

I. INTRODUCTION

Although Rayleigh-Taylor instability experiments have long been used to characterize solid strength at high strain rates and pressures [1–4], Richtmyer-Meshkov instability (RMI) experiments were only more recently proposed to study strength [5–7]. Since then, to exploit the strong sensitivity of RMI to strength, experiments have been fielded in various configurations [8–20]. This work uses experiments with perturbations on a free surface, e.g., Refs. [9,21], which are most sensitive to strength at relatively low pressures and strain rates of $\sim 10^7$ s^{-1}. When combined with other experiments, free-surface RMI experiments allow one to largely isolate strain rate effects on strength from pressure effects [22,23]. Further, we use impact loading, e.g., Ref. [24], rather than high explosives, to better control the loading conditions and for simpler experiments.

RMI experiments are well suited to contribute unique information to an open question in the literature. A large increase in strength at strain rates of 10^3-10^5 s^{-1} for metals has been inconsistently observed in the literature. For copper, some have observed this upturn [25–30], and others found no significant upturn [31–34]. Rosenberg *et al.* [35] critically

reviewed the discrepancy and identified possible explanations. Comparing different techniques, especially those that might include effects of higher pressures on strength, was a major concern. Indeed, a careful correction for pressure effects on aluminum strength measurements resulted in the apparent onset of strong rate sensitivity being shifted nearly three orders of magnitude, from $\sim 10^4$ to $\sim 10^7$ s^{-1} [36]. Rosenberg *et al.* [35] contended that experimental details with Split-Hopkinson pressure bar (SHPB) testing such as direct impact contribute to data scatter that made conclusive identification of the upturn difficult. In the end, Rosenberg *et al.* [35] still recommended SHPB testing to study the upturn because it does not have the pressure effect but with higher strain rates being achieved via smaller specimens (e.g., [37–40]). Lea and Jardine [41] employed direct impact SHPB testing on copper to provide the highest signal-to-noise evidence of the upturn yet reported. They showed an upturn starting at 10^4 s^{-1} with an ultimate threefold increase in strength, the highest yet reported with SHPB testing. That peak value came at 1.5×10^5 s^{-1}. The copper RMI experiments in this paper will extend that maximum strain rate by more than two orders of magnitude and compare the strength results to literature data on the strength upturn.

To isolate strain rate effects on strength, we make use of an important observation about changing the length scale of RMI perturbations, as shown in Fig. 1. The initial size of the perturbation is characterized by the nondimensional amplitude $\eta_0 k$, where η_0 is the sine wave amplitude, and the wave number $k = 2\pi/\lambda$, where λ is the wavelength. The Richtmyer equation [4,42,43] shows that the growth rate of the perturbation amplitude is independent of the length scale

---
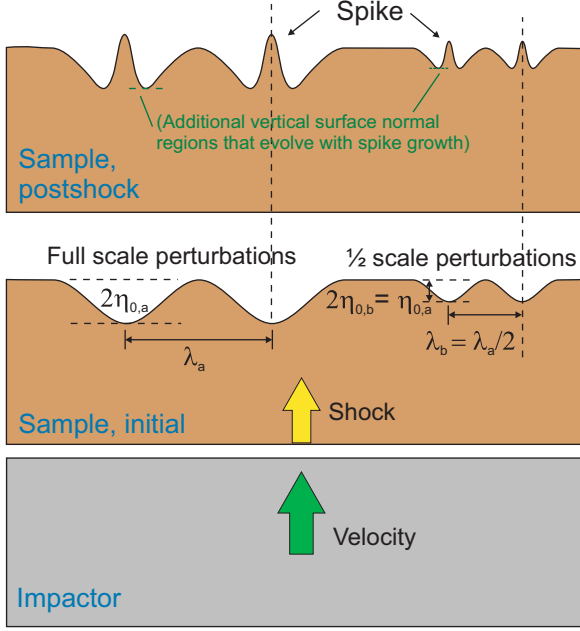
FIG. 1. Simplified illustration of a multiscale Richtmyer-Meshkov instability (RMI) experiment with full and half-scale perturbations on the left and right, respectively. The deformed shape on the top represents the time of maximum spike velocity for an instability that eventually arrests. Note that, because of the different strain rates, the self-similar postshock shapes would occur at different times. The indicated vertical surface normal regions in addition to the original high and low spots appear prominently in the experimental data later in the paper. (Illustration not to scale.)

of the perturbations:

$$\frac{d\eta}{dt} = (\eta_0 k) A \Delta u, \tag{1}$$

since $\eta_0 k$ is dimensionless. Here, Δu is the impulsive velocity jump for the shock, and A is the Atwood number for the two materials, which is -1 in our case with a free surface. The resulting negative growth rate indicates that the perturbations will invert.

To get from growth rate to a representative strain rate, both sides of the Richtmyer equation are divided by the initial perturbation amplitude which, ignoring the sign, gives the proportionality [44]:

$$\dot{\varepsilon} \propto \frac{\eta_0 k}{\eta_0} \Delta u = k \Delta u, \tag{2}$$

which now introduces a length scale. The strain rate scales inversely with the perturbation wavelength.

The Richtmyer equation only considers the behavior of a fluid. To better capture the instability behavior of a solid with strength, Piriz *et al.* [6] developed an equation of motion where stress acts on the interface and potentially arrests the instability. Buttler *et al.* [9] elaborated on this equation and showed that the time and spatially varying strain rate in the perturbation takes the form [45]:

$$\dot{\varepsilon} \propto \frac{(\eta_0 k)}{\lambda} f(x, y) g(t) \Delta u, \tag{3}$$

where rather than substituting k, we have kept λ in the denominator because it is convenient for discussing length scale.

Equation (3) shows that, at any time and location within the instability, the strain rate scales with $(\eta_0 k)/\lambda$, which suggests the experimental plan for the work reported here. Making use of the self-similar growth behavior, hold $\eta_0 k$ constant to keep the amount of deformation, i.e., plastic strain, approximately equal. Thus, strain rate effects can largely be isolated by scaling the initial perturbations up and down in scale by changing λ. This scaling is illustrated schematically in Fig. 1 for scaling by a factor of two. The key to further isolating strain rate is to put separate perturbations with different wavelengths on a single target so they see identical shock loading Δu, which also helps keep the deformation nearly constant. Thus, only the strain rate changes significantly between the different perturbations on a single target. Finally, the experiment can be repeated for different $\eta_0 k$ to test the scaling by $\eta_0 k$ predicted by Eq. (3) but not Eq. (2).

II. EXPERIMENTAL METHODOLOGY

Three gas gun RMI experiments were designed to isolate the effect of strain rate on strength using Eq. (3). The target for each individual experiment had three regions of sine wave perturbations with the same $\eta_0 k$, but the dimensional scale, i.e., λ, spanned a factor of about five. The three targets then had different values for $\eta_0 k$ to explore different levels of instability growth and the resulting plastic strain. The remainder of this section provides the details about the targets and the gas gun experiments.

A. Sample preparation

RMI targets were machined as 3-mm-thick by 60-mm-diameter disks from OFHC Cu that was annealed at a temperature of $600\,°C$ for 1 h. This Cu has equiaxed grains with an average grain size of $60\,\mu m$. The microstructure of this batch of Cu has been extensively characterized and reported previously [46]. Each disk had three different perturbation zones with the same $\eta_0 k$ but varying wavelengths of 65, 130, and $320\,\mu m$. The zones on each target were designed to be $\sim$6.5 mm wide separated by 10 mm flat regions, as shown in Fig. 2. Three targets had $\eta_0 k$ of 0.3, 0.6, and 0.9.

Due to the complexity of the design, RMI targets had to be machined one at a time rather than simultaneously as in some previous work [24]. A diamond turning air bearing spindle with a balanced fly cutter was set up for this purpose. In this setup, the tools could be changed easily. The individual targets were placed on top of the Z-axis tool holder with a custom chuck matched to the diameter of the sample. A large-radius diamond tool was used to fly cut the first side to a diamond flat surface. Then the part was flipped in the vacuum chuck and faced down to thickness with the same large radius tool. Then the tool was changed to the maximum tool radius that could fit inside the sine wave profile and touched off on the surface to set the zero height. Each program was set up to iterate the sine wave fly-cutting operation down into the part one sine wave region at a time and then move on to the next region.
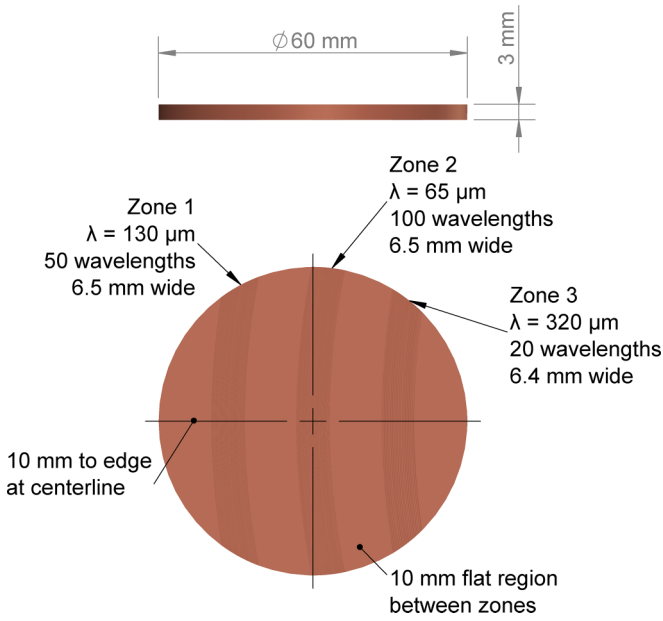
FIG. 2. Each copper target had three regions with the same $\eta_0 k$ but with different λ.

FIG. 3. Map of photon Doppler velocimetry (PDV) probes overlaid on photograph of specimen. Each perturbation region had one of each probe size. Scaling for the probes in the figure is approximate.

The annealing heat treatment was repeated after machining to remove any work hardening near the surface.

After machining, the targets were inspected on a coordinate measuring machine using a Zygo white light interferometry probe to measure the profile for each of the nine total perturbation regions. The profiles generally follow a sine wave profile very well, with the roughest profiles coming from the smallest $\eta_0 k$ at the smallest λ. Wavelengths and peak-to-valley depths were taken from each profile to compare with the design. For all nine perturbation regions, the wavelengths fell within $\pm 0.6\%$ of nominal. For 8 of 9 regions, η_0 fell within $\pm 4\%$ of nominal. For $\eta_0 k$ of 0.3 at $\lambda = 65\,\mu\text{m}$, the nominal η_0 is only $3.1\,\mu\text{m}$, and the actual was 10% high at $3.4\,\mu\text{m}$. Overall, the variations were randomly distributed and are too small to significantly affect the behavior, so for simplicity, nominal values were used later in the data analysis.

B. Velocimetry

Photon Doppler velocimetry (PDV) is a velocity diagnostic ideally suited to RMI measurements, as it can measure multiple velocities simultaneously. A laser is used to illuminate a surface, and the reflected light is collected. Any motion of that surface introduces a shift in the frequency of the collected light, from which the velocity can be calculated [47]. The instability evolution in RMI experiments generates a range of surface velocities, and each of these frequency shifts can be resolved from the PDV data from a single laser using a Fourier transform approach. The spectrogram produced with the Fourier analysis will identify these multiple frequencies with intensities related to the amount of light collected from each reflective area travelling at that velocity.

However, there are some experimental features that make PDV challenging to use with RMI. First, the varying angle of the sinusoid perturbations and the character of the precision machined surface both diffuse the collimated laser light,
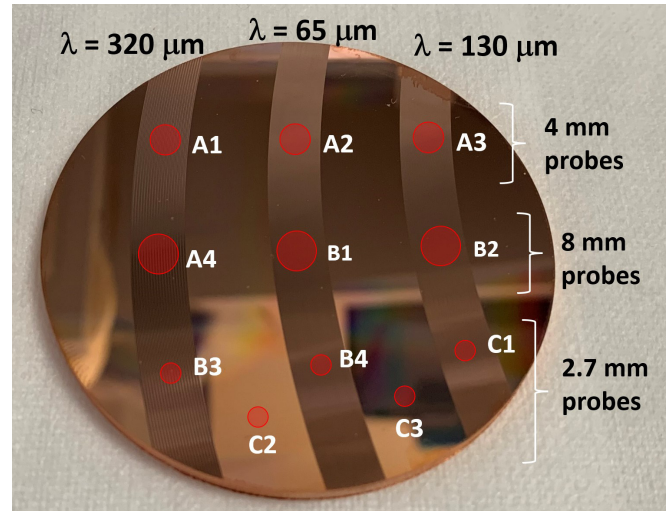
reducing the amount of light that is reflected directly toward the PDV probe. The light is typically delivered to the target surface using a small collimating probe, with a beam diameter on the order of hundreds of microns. Due to this small packaging of typical PDV probes, they are very inefficient at coupling light back into the optical fiber unless the path is normal to the probe. This can be solved with larger probes, especially with focusing lenses, but that makes fitting many points on a typical RMI experiment difficult or impossible. Increasing the amount of light sent to the target can help, but there are limits on the amount of light before either the optics or even the sample is damaged. Secondly, we are primarily interested in the spike velocity. The width of the spike tip is a fraction of the original perturbation wavelength, as seen in Fig. 1, further reducing the amount of light collected in the main area of interest. Usually, there is some tolerance between the hole for the probe and the probe body, and the probe is moved until the amount of reflected light being collected is maximized. However, these adjustments must be modest to make sure that the light return is still from the desired location.

In this paper, larger collimating probes were used to try to capture the full spectrum of velocities from even the large wavelength perturbations. The probe body diameters were 2.7, 4, and 8 mm. With these probes, the beam necks down to its minimum value at the working distance but in this paper are used closer to the surface for better light return. The laser spot size on the target varies as the surface moves but is typically about half the probe diameter. The probe body diameter will be used to identify which probe is being referred to from here on. A map of the different probe locations is shown in Fig. 3—each perturbation wavelength had one of each probe type to compare signal quality. Probes C2 and C3 in the map were used to measured velocity in flat regions. An additional probe was used to measure the impactor velocity. A 1550-nm-wavelength laser was used.

C. Execution

Three plate impact experiments were performed on these targets using an 80 mm bore single-stage light gas gun. The Cu targets were bonded into a Lexan plate 152.4 mm wide by 127 mm high and 12.7 mm thick to allow for mounting and alignment in the gas-gun target tank. The impact face of the samples, i.e., the side with no perturbations, was protruding 0.4 mm from the Lexan plate. To ensure a planar impact between the projectile and the target, a mirror was affixed to the front of the target, and a laser was used to align a spot down and back along the 9.2 m barrel. With this method, the deviation from parallel at impact is typically submilliradian. The flyer plates were tantalum, 50 mm diameter by 2.03 mm thick, affixed to the front of a Lexan projectile.

The measured impact velocities were 976, 959, and 966 m/s, all ± 1 m/s, for the $\eta_0 k$ 0.3, 0.6, and 0.9 targets, respectively, a total spread of <2%.

III. ANALYSIS AND MODELING METHODS

The RMI experiments provide a wealth of data: the velocity time histories of all the surfaces that return sufficient light to the probe. There is a spectrum of ways to use the data to evaluate strength. At one end of the spectrum, the full velocity histories can be used, for example, in a Bayesian inference framework to calibrate parameters in a strength model and a damage model as well, e.g., Ref. [48], since at late time, the instabilities are also affected by damage. Such an effort on these data is in progress and will be reported in future work. Instead, in this paper, we quantify a representative average strength Y from each perturbation region on each experiment. To isolate strength effects from damage, the estimation calibrates on the maximum spike velocity, an early time experimental metric that is only affected by strength [21]. The average strength approach gives quantified strength estimates that can reveal trends over the varying conditions. Furthermore, quantified strength estimates can be compared with strength estimates from other techniques in the literature to potentially reveal important trends. Notably here, we will also estimate $dY/d(\ln \dot{\varepsilon})$, the rate of change of the average strength with respect to the log of the strain rate.

A. Strength estimation

An average von Mises effective strength Y in each experiment was estimated by matching hydrocode simulations to data using an established methodology [21,24], which is summarized here. The experiments were modeled using FLAG, an arbitrary Lagrangian/Eulerian, explicit, finite-volume hydrodynamics code using arbitrary polyhedral computational zones [49–53]. No mesh relaxation or Eulerian remapping was used in these calculations because all the deformations were modest in the time of interest. The computations used a two-dimensional plane strain mesh on a cross-section through the perturbation, the section shown in Fig. 1. A $1-\lambda$ domain with symmetry boundary conditions, which effectively assumes infinitely repeating perturbations, was used. The impactors were initialized with the experimentally measured velocities from Sec. II C and then impacted the target with a contact surface. The calculations used a classic VonNeumann and Richtmyer

(VNR) viscosity with a quadratic coefficient of 1.2 and a linear coefficient of 0.15 [54]. Numerical viscosity artificially reduces the predicted spike velocities, but the effect converges away [21], so the strength estimates used peak spike velocities from meshes with zone sizes of $\lambda/40$, $\lambda/80$, and $\lambda/160$ and then a linear best fit of those values extrapolated to a zero zone size.

The tantalum impactors were modeled using an extensively calibrated model for tantalum [22], including the 93524 SESAME equation of state [55] and a Preston-Tonks-Wallace strength model [56]. The copper was modeled using SESAME equation of state 3337 [57] and an accompanying temperature- and pressure/density-dependent shear modulus [58]. Simple one-dimensional impact simulations of each experiment matched the velocities on the flat regions of the target to well within the expected 1% uncertainty of the measured impact velocities, validating the model setup. For the strength estimation, an elastic, perfectly plastic, i.e., constant strength, model was used for the copper. Calculations were repeated with strengths from $Y = 400$ to 1600 MPa in increments of 200 MPa, and then the predicted maximum spike velocities were compared with the experimental data to interpolate to the strength value that best matched the data.

B. Maximum velocity extraction

Velocity-time spectrograms were produced from the data using SIRHEN [59]. Because of limited signal-to-noise in many of the spectrograms, an automatic algorithm for extracting the maximum spike velocity [60] was unable to consistently identify the maximum. Therefore, maximum spike velocities were extracted manually from the spectrograms. The surfaces that are oriented normal to the PDV laser tend to return significantly more light, so the spike tip tends to return a distinct and easily identified signal. In cases where the signal-to-noise ratio was poor or the signal dropped out for short periods of time, the expected shape of the spike velocity curve (see Fig. 7 in Ref. [24]) was used to help identify the maximum. Because of this heuristic process, conservative estimates of uncertainties were assigned individually based on the quality of each signal. The extractions were done blindly, without knowledge of which spectrogram went with which probe, to minimize any unconscious biases affecting the results.

C. Physical regime sensitivity

Interpreting the average strength estimates and comparing them with other measurements from the literature requires knowing the strain rate. The recently developed physical regime sensitivity (PRS) analysis technique [61] is ideally suited to estimate a representative strain rate. Compared with conventional sensitivity to model parameters that affect a broad range of conditions, PRS isolates model sensitivity to local regimes of independent variables like strain rate.

In PRS calculations, the model of interest is perturbed in specific regimes of independent variables that the model depends on. In this application, our model of interest is strength, and the independent variable being examined is strain rate. The strength model used here is the same elastic, perfectly

plastic model used for strength estimation, with the strength Y for each λ set as the value reported later in this paper that best matched the experiments. The perturbation to the flow stress is implemented as a Gaussian function multiplier that is centered on a specific value, or target, of the strain rate such that the flow stress will always be slightly increased when the strain rate in the simulation is near that target [62]. Here, the strength was increased by 10% with a Gaussian width of 0.1 on the log of the strain rate since strength generally increases with the log of strain rate. The perturbed simulation is then compared with the unperturbed simulation, and the sensitivity is the percent change in the experimental metric being considered, which is the maximum spike velocity in this paper. PRS curves were constructed by a series of simulations varying the target for the log of the strain rate (in s^{-1} units) from 4.0 to 9.0 in increments of 0.05. The calculations were repeated for all nine combinations of λ and $\eta_0 k$ to generate a PRS curve for each case.

To obtain a single representative strain rate value from a PRS curve, we find the centroid, an average where each target log strain rate is weighted by the absolute value of the corresponding sensitivity.

IV. RESULTS AND DISCUSSION

A. Experimental results

The two smaller diameter probes produced a far better signal-to-noise ratio than the 8-mm-diameter probe. We hypothesize that this was due to the poor collection efficiency between the larger diameter reflected beam and the very small diameter of the optical fiber core (9 μm) used to then send the light to the PDV system. Hence, while a large area of the sample was interrogated using the bigger diameter probes, much of the reflected light was then wasted. The 2.7 and 4 mm probes generally returned good quality spectrograms with readily identifiable maximum spike velocities, and both are used for further analysis.

Two PDV velocity spectrograms with better-than-average signal-to-noise are plotted to best illustrate key features in the results. Figure 4 shows a spectrogram for $\eta_0 k = 0.9$ and $\lambda = 320$ μm. Close examination shows two distinct shock arrivals separated by ~19 ns, which correspond to arrival at the low and high points of the perturbations. After shock arrival, the wide range of simultaneous velocities indicates perturbation growth. The dominant velocities at ~900 m/s come from the original high spot of the perturbation, which is called the bubble in the literature for fluids, although that terminology is less appropriate for solids with strength [63]. The dominant velocity peaking at 2300 m/s is the spike. An intermediate dominant velocity region, starting at ~1700 m/s and decaying down to ~1100 m/s, corresponds to the new low spot that evolves on either side of the spike in the postshock portion of Fig. 1. The spike velocity pulls back significantly, an effect of strength, to ~1700 m/s. However, the spike velocity stays well above the bulk postshock velocity of ~1150 m/s, indicating that the perturbation went unstable, and part of the spike broke off. Behind the spike, the rest of the velocities come together ~0.3 − 0.4 μs after shock arrival, indicating no further instability growth. At ~1.6 μs, a dip in the
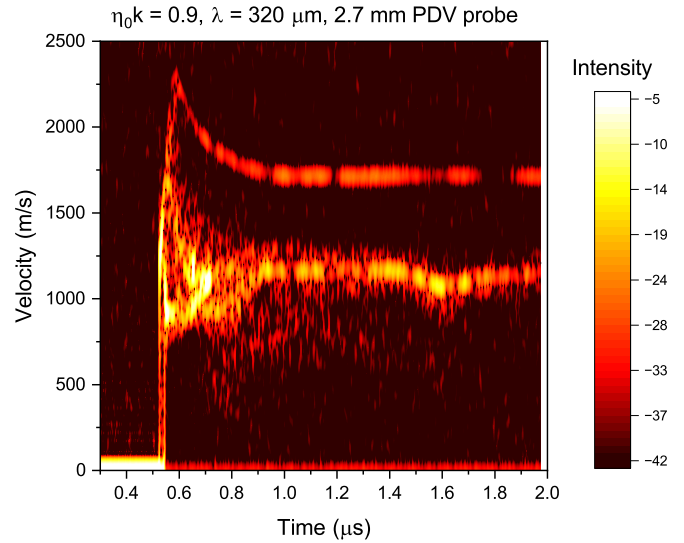
FIG. 4. The photon Doppler velocimetry (PDV) velocity spectrogram for $\eta_0 k = 0.9$ and $\lambda = 320$ μm with the 2.7-mm-diameter probe shows a wide range of velocities after shock arrival and an instability as evidenced by separate velocities at late time.

1150 m/s velocity signal corresponds to a macroscopic spall layer that is well below the surface.

Figure 5, a spectrogram for $\eta_0 k = 0.6$ and $\lambda = 65$ μm, shows key differences compared with Fig. 4. The peak spike velocity only reaches ~1760 m/s because of the smaller initial perturbation amplitude. All the velocities come back together, indicating full arrest and no instability. That occurs ~0.05 μs after shock arrival, much faster than in Fig. 4, consistent with the shorter time scales and higher strain rates for the smallest wavelength case. The small dip in the velocity at
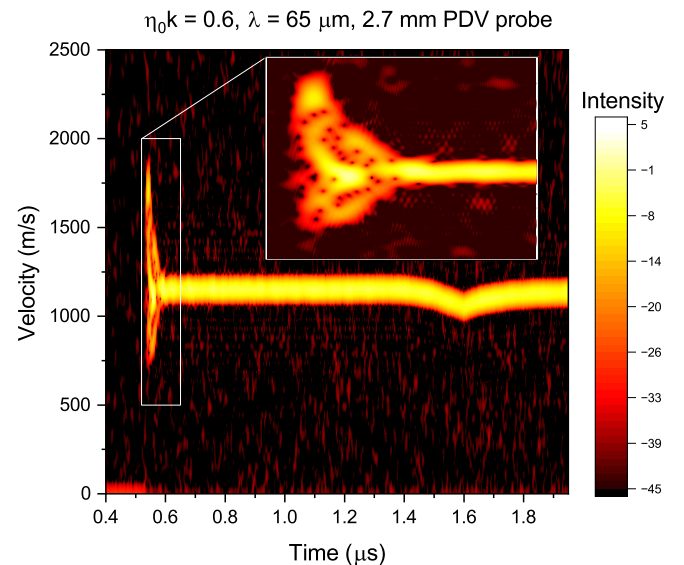
FIG. 5. The photon Doppler velocimetry (PDV) velocity spectrogram for $\eta_0 k = 0.6$ and $\lambda = 65$ μm with the 2.7-mm-diameter probe shows a lower peak velocity, no instability, and everything occurring on a smaller time scale than Fig. 4. The inset shows that the shorter time spike evolution and arrest is still captured.
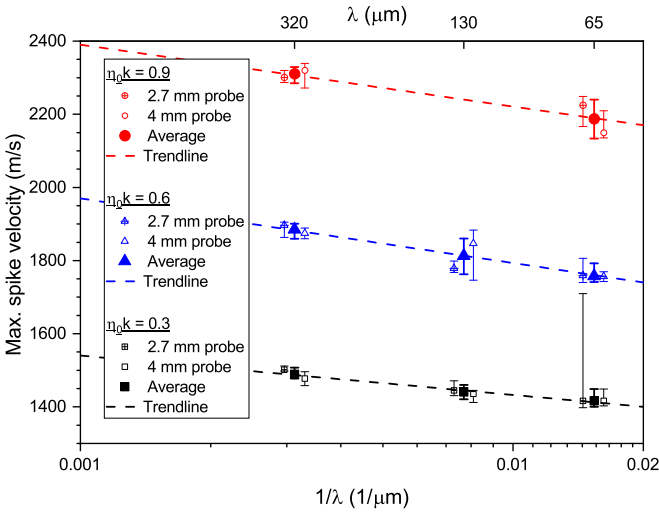
FIG. 6. The measured maximum spike velocities plotted vs $1/\lambda$ (a proxy for strain rate, plotted on a log scale) decrease as λ decreases, consistent with an increase a strength as the strain rate increases.

FIG. 7. The average strengths estimated from the multiscale Richtmyer-Meshkov instability (RMI) experiments show $\sim$70% strength increase with decreasing wavelength but no significant trends as a function of increasing $\eta_0 k$, which increases the plastic strain.

1.6 µs is essentially like Fig. 4 since it reflects macroscopic spall behavior.

The Supplemental Material [64] shows spectrograms for both probes on each perturbation region in all three experiments and shows maximum spike velocities with uncertainites (it also includes raw oscilloscope data for all probes). Unfortunately, none of the probes on the $\eta_0 k = 0.9$ region at $\lambda = 130$ µm gave sufficient light return to identify the maximum spike velocity. Unstable perturbation growth only occurred for $\eta_0 k = 0.9$ with $\lambda = 130$ and 320 µm. Thus, the transition to instability occurred when λ increased from 65 to 130 µm, presumably because of a strength decrease at the lower strain rates.

Figure 6 shows the maximum spike velocities plotted vs $1/\lambda$, a proxy for strain rate per Eq. (3), on a log scale because strength tends to increase proportionally to the log of the strain rate. The average between the two probes is also plotted along with a combined uncertainty. The velocities decrease with decreasing λ, averaging about a 6% decrease from 320 to 65 µm. A decrease in maximum velocity for a fixed $\eta_0 k$ indicates

increased strength suppressing the instability growth. Table I gives the values plotted in Fig. 6.

B. Strength estimations

Figure 7 shows the average strengths, estimated from the average velocities in Fig. 6, for each perturbation region in the RMI experiments. The $\eta_0 k = 0.3$ region has the highest strength uncertainties despite having the lowest average-velocity uncertainties because the smaller perturbations have significantly lower sensitivity to strength.

Because larger $\eta_0 k$'s experience more plastic strain, significant strain hardening effects would appear as higher strengths for higher $\eta_0 k$'s. No such trends are apparent. Therefore, the average strength estimated for each λ by simultaneous fitting to all three $\eta_0 k$'s provides the most robust strength estimate and is used in further analysis. That estimated strength increased by $\sim$70% from the largest to smallest wavelength.

TABLE I. Maximum spike velocities.

| λ | $\eta_0 k$ | Maximum spike velocity (m/s) | | |
		2.7 mm PDV	4 mm PDV	Average
65 µm	0.3	$1417 + 293 - 19$	$1417 + 32 - 14$	$1417 + 32 - 17$
	0.6	$1759 + 47 - 19$	$1757 + 13 - 14$	$1758 + 35 - 17$
	0.9	$2225 + 24 - 58$	$2149 + 60 - 14$	$2187 + 53 - 53$
130 µm	0.3	$1445 + 26 - 14$	$1436 + 9 - 24$	$1441 + 19 - 20$
	0.6	$1779 + 20 - 11$	$1847 + 37 - 100$	$1813 + 48 - 15$
	0.9			
320 µm	0.3	$1501 + 10 - 4$	$1477 + 19 - 19$	$1490 + 17 - 12$
	0.6	$1896 + 9 - 33$	$1875 + 14 - 15$	$1886 + 15 - 26$
	0.9	$2300 + 19 - 14$	$2320 + 19 - 48$	$2310 + 19 - 25$
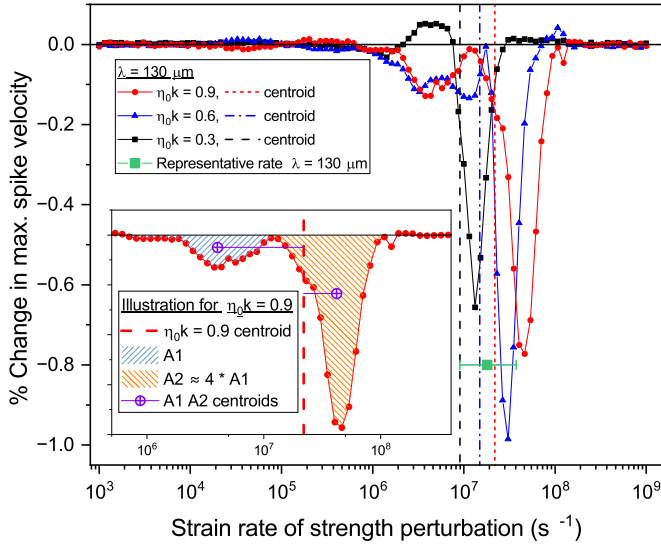
FIG. 8. The physical regime sensitivity (PRS) curves for the example of $\lambda = 130\,\mu$m show dominant negative sensitivity peaks between 10^7 and $10^8\,$s^{-1}. The centroid for each curve also accounts for mild sensitivities at lower rates, as illustrated in the inset. Since the strength estimate uses data from all three $\eta_0 k$'s, a weighted average gives an overall representative strain rate for this λ.

C. PRS

Figure 8 shows the PRS strain-rate curves for all three $\eta_0 k$'s for $\lambda = 130\,\mu$m. The sensitivities are predominantly negative because the PRS calculations increase the strength, which tends to reduce the maximum spike velocity. Each curve has one dominant (negative) sensitivity peak that occurs between 10^7 and $10^8\,$s^{-1}. Examination of the simulation results shows that those strain rates occur in the central region of the spike near the tip, where the largest plastic strain accumulates, as shown in Fig. 6a in Ref. [65]. Modest sensitivities arising from other regions of the perturbations persist down to $\sim 10^6\,$s^{-1} and bring the calculated centroid somewhat counterintuitively left of the dominant peak. The inset in Fig. 8 shows that, for the example of $\eta_0 k = 0.9$, the overall centroid approximately balances the area times the distance to the centroids of the two largest peaks.

Since each strength estimate used all three $\eta_0 k$'s, a single representative strain rate and associated uncertainty was calculated heuristically from the three PRS curves. The overall sensitivity of data from each $\eta_0 k$ to strength is given by the area under the PRS curve and was verified independently from the differences between the constant Y simulations used for estimating strength. The $\eta_0 k = 0.3$ data have lower overall sensitivity, partly because of positive sensitivity regions $<10^7\,$s^{-1}, as in Fig. 8, with the overall sensitivity being 2.5–3.5 times greater for the two larger $\eta_0 k$'s. The overall sensitivity acts as weighting in the simultaneous fit of strength and should also be used in weighting the combined centroid. In log space, the average of the centroid locations for the two larger $\eta_0 k$'s falls within 0.5% of the weighted averages of all three centroids and is thus taken as the representative strain rate. To provide a conservative estimate of one standard deviation uncertainties, the positive uncertainty extends to the

TABLE II. Average strength estimates from the copper RMI experiments and the associated strain rates and strains estimated by PRS. The uncertainty on the strain rate can be represented with an uncertainty on $\log_{10} \dot{\varepsilon}$ of ± 0.33, which should be used to simultaneously shift all three points, keeping the relative positions intact.

$\lambda(\mu$m)	Average Y (MPa)	Strain rate (s^{-1})[$\log_{10}$]	Strain
320	$700 + 75 - 50$	8.7×10^6 [6.94]	$0.48 + 0.1 - 0.2$
130	$1000 + 100 - 100$	1.8×10^7 [7.26]	$0.45 + 0.1 - 0.2$
65	$1190 + 50 - 50$	3.3×10^7 [7.52]	$0.42 + 0.1 - 0.2$

midway between the dominant peaks for those larger $\eta_0 k$'s. The negative uncertainty extends to the centroid location for $\eta_0 k = 0.3$.

The PRS strain rate curves for the other λ's are quite similar to Fig. 8, and the uncertainties in each case can be represented with an uncertainty on $\log_{10} \dot{\varepsilon}$ of ± 0.33. This relatively large uncertainty in Fig. 8 represents the uncertainty in how one assigns a representative value. Having defined that and applied it consistently, the relative uncertainty between the representative strain rate values for the three λ's is smaller by roughly an order of magnitude, which should allow for a reasonable estimation of $dY/d(\log_{10} \dot{\varepsilon})$.

PRS curves were also generated to identify the regime of sensitivity for strain as the independent variable in the strength model. Representative values and uncertainties for strain were arrived at using similar heuristics as for strain rate. The associated centroids for strain are reported in Table II. The representative strain decreases modestly from 0.48 for $320\,\mu$m to 0.42 for $65\,\mu$m because the increased strength at the smaller wavelengths reduces the deformation. These are representative centroid values. The larger perturbations show significant sensitivities out to strains as high as 0.9.

D. Results summary

Table II gives the simultaneous-fit strength estimates and uncertainties from Fig. 7. The associated strains and strain rates are the representative values from the PRS analyses. From these values and all the associated uncertainties, the best fit $dY/d(\log_{10} \dot{\varepsilon})$ is $830 \pm 160\,$MPa $\cdot \log_{10}($s$)$, assuming a linear relationship.

E. Strength upturn and mechanisms

Although differing conditions and loading paths preclude a perfect comparison [66], plotting our RMI strength estimates vs strain rate along with copper data from conventional quasistatic and SHPB constitutive testing is still an informative way to put the results in a broader context. Figure 9 shows such a comparison with testing on our batch of copper along with data from the literature on other copper [26,28,33,34,38,41]. The horizontal uncertainty bar on the middle RMI strength estimate is the estimated group uncertainty in the strain rate estimate discussed previously, so the relative uncertainties and the plotted best fit slope are much less uncertain. The steep dependence of the RMI strengths on strain rate is striking at just over twice the steepest slope
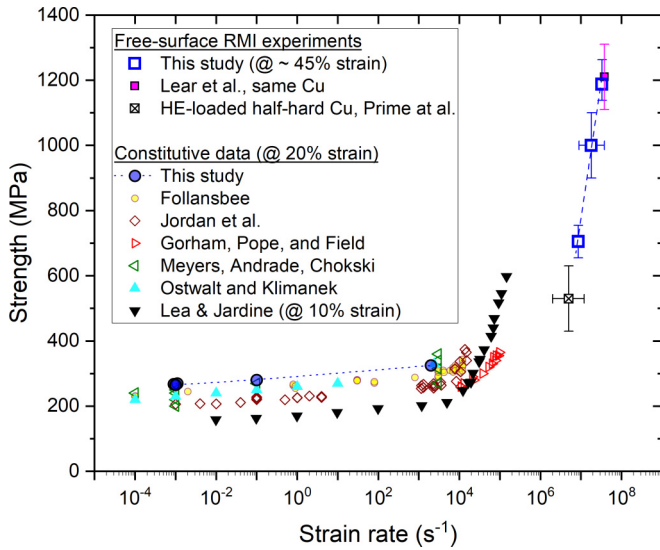
FIG. 9. The Richtmyer-Meshkov instability (RMI) strength estimates show a steep dependence on strain rate that agrees well with extrapolations from some of the constitutive data in the literature. The different datasets represent varying amounts of plastic strain so should be interpreted with caution. Also, the literature data come from source materials with different microstructures.

FIG. 10. Room-temperature (unless noted) quasistatic testing of copper recovered after a shock shows hardening beyond that expected just from the accumulated strain from the shock and unload cycle, which has been used to offset the postshock curves.

shown by Lea and Jardine [41] at lower rates. At least to some extent, the RMI results support the strength upturn measured by some previous researchers. The RMI data appear to be offset from an extrapolation of Lea and Jardine [41]. Qualitatively, the RMI data only appear to be a consistent extrapolation from the Gorham *et al.* [38] data. However, directly comparing details of the strength trends of data on different sources of copper with different microstructures is likely misleading. Indeed, Jordan *et al.* [28] found that correcting the data for variations in grain size collapsed much of the data into more consistent agreement. Unfortunately, Gorham *et al.* [38] did not report their grain size.

The RMI copper experiences shock hardening, but the constitutive testing does not, which affects the comparison. For a 25 GPa shock in copper, the shock and unload cycle produces an equivalent strain of ∼17%, as calculated conventionally by $\frac{4}{3}\ln(V/V_0)$. Because the hydrocode simulations for the PRS analysis automatically track the accumulated strain, that 17% is implicitly included in the representative strains in Table II that are ∼45%. However, copper experiences enhanced shock hardening, meaning hardening beyond that expected from the 17% of plastic work strain. In Fig. 10, the stress-strain response of shocked copper, measured quasistatically after recovery [67,68], has been offset by the cyclic strain for that shock level. With the quasistatic reloading, the yield strength increases, but the subsequent work hardening decreases compared with unshocked material strained to the equivalent level because the hardened microstructure recovers [67,69,70]. However, at RMI rates, recovery is less likely. For a 20 GPa shock, the yield stress in Fig. 10 increases an additional ∼80 MPa. Extrapolating slightly to a 25 GPa shock, the yield stress should increase by ∼100 MPa, the level of the RMI errors bars in Fig. 9. In the end, the RMI are an average strength centered at the representative strains
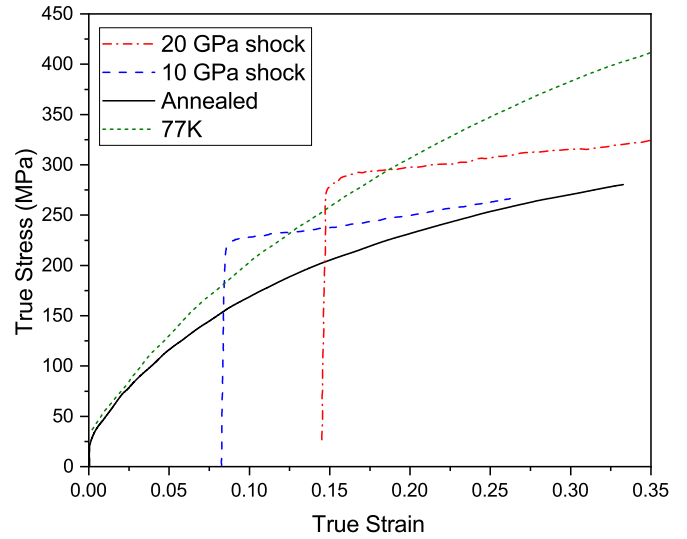
in Table II. Strain hardening in annealed copper at rates up to 10^4 s^{-1} starts to level off after ∼20% strain, and the RMI data at higher rates did not show measurable strain hardening, so strain hardening past 20% strain probably has modest effect on the average. All told, strain hardening including shock hardening probably does not significantly affect the comparison in Fig. 9 other than the Lea and Jardine [41] data at only 10% strain.

The experiments $> \sim 1$ s^{-1} strain rate include adiabatic heating. The heating increases monotonically as strength increases. The 25 GPa shock causes an additional ∼45 K of residual temperature increase for the RMI experiments. While that makes the comparison less precise, the effect is not significant on the scale of Fig. 9.

Two additional RMI data points from separate experiments are also plotted. The experiments in Ref. [65] were very similar to this paper, using the same copper, a 65 μm λ, and a tantalum impactor but with ∼12% higher impact velocity, which was used to scale the representative strain rate using Eq. (3). The strength of 1210 MPa (from Fig. 7(c) in Ref. [65], for the undoped control specimen) is plotted in Fig. 9 and is consistent with our high-rate result. For the high-explosive driven RMI experiment in Ref. [21], strain rates from Fig. 16 were compared with the simulations in this paper to estimate an equivalent centroid of ∼5×10^6 s^{-1}. Plotted in Fig. 9, the apparently modest strength estimate of 530 ± 100 MPa from Ref. [21] then makes sense because of the lower strain rate. Considering the approximate estimate of strain rate and that Ref. [21] used half-hard copper as compared with annealed, the precise agreement with the trend seems somewhat fortuitous.

Other copper RMI experiments in the literature seem to give lower strengths but cannot be compared directly in Fig. 9 because of the inability to simply estimate a representative strain rate and because the strength estimates used different

approaches, which hinders a fair comparison. The HE-loaded experiment in Ref. [9] is very similar to the experiment in Ref. [21]. They report a strength estimate of 370 MPa using a very different analysis based on total spike growth at arrest measured radiographically. One can expect the representative strain rate for that experiment to be lower than for Ref. [21] since the strain rate decreases in the time between maximum spike velocity and arrest, thus bringing down the average strain rate. Also, a strength based on total spike length in the free-surface configuration might be artificially low because of the effects of tensile damage and porosity [21]. An experiment tamped to give pressures up to 10 GPa that also used imaging to measure spike growth [16] gave a strength estimate of 470 MPa at strain rates reported as $10^7 \, \mathrm{s}^{-1}$ and below. Similar untamped experiments by the same group [71] gave a strength estimate of ∼500 MPa for strain rates reported as peaking at 10^7-$10^8 \, \mathrm{s}^{-1}$. Other experimental methods that might give low-pressure strength at rates comparable with RMI are under development [72].

Few of the extreme-rate, non-RMI experiments on polycrystalline copper in the literature report strengths much above our maximum strength despite higher pressures during the experiments. Recovered instability experiments inferred a strength of ∼700 MPa at a reported strain rate of $2 \times 10^7 \, \mathrm{s}^{-1}$ and a pressure of 5 GPa but with an uncertainty on the strength estimate extending to >2 GPa [73]. Pressure-shear experiments gave copper strength up to 1 GPa at a pressure of 42.5 GPa and a strain rate of $\sim 10^5 \, \mathrm{s}^{-1}$ [74]. Figure 7 in Ref. [74] shows that various measurements gave conflicting results, with Ref. [75] reporting a strength of ∼1 GPa at ∼100 GPa pressures using symmetric shock release experiments compared with ∼1.5 GPa by Ref. [76] using similar methods, but measurements using transverse stress gauges under shock loading gave copper strengths of ∼1.2 − 1.3 GPa for peak states of only 4–11 GPa [77]. Diffraction measurements under laser compression gave a strength of 1.75 GPa at only ∼32 GPa pressure [78]. Since pressure-scaling effects defy simple modeling assumptions [23,74], no attempt is made here to bring these measurements to a common pressure for comparison with the RMI data. Other extreme experiments such as ramp release [79] and Rayleigh-Taylor [80] interrogate strengths at even higher pressures and might well give higher strengths, but no results are reported for copper.

One might question if the strength upturn in Fig. 9 indicates a transition to a viscous phonon-drag mechanism. Such a transition should result in the strength of the metal increasing with temperature, which is very different behavior than the thermal softening seen in the thermally activated regime of dislocation motion [81]. Lea and Jardine [41] observed no thermal hardening at temperatures up to 600 K, thus phonon-drag effects were unable to explain their increase in strength starting at $10^4 \, \mathrm{s}^{-1}$. They were able to show rather that the strengthening was consistent with the time limited self-organize criticality of dislocation avalanches [82,83]. That mechanism should also result in an increasing rate of work hardening with strain rate. For our RMI results, no significant strain hardening is distinguishable in Fig. 7, and the lack thereof could be consistent with a transition to a different mechanism like phonon drag at the higher rates accessed in this paper, but it is not clear if the
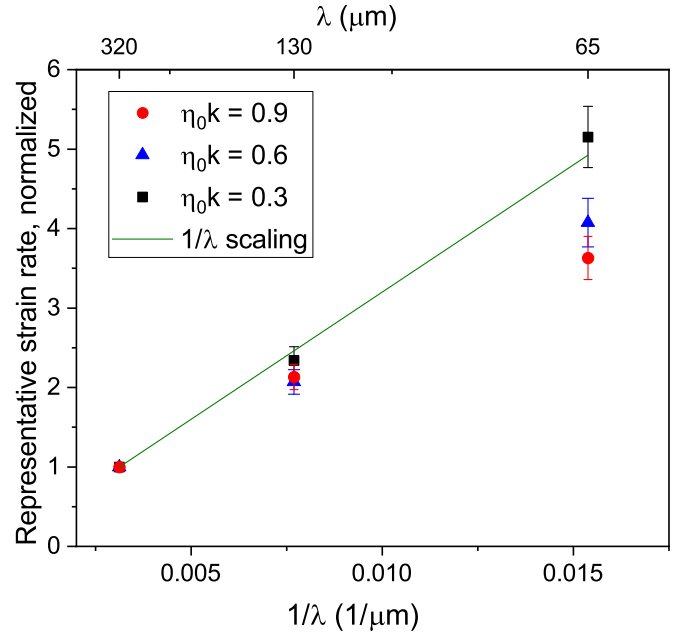
FIG. 11. The physical regime sensitivity (PRS) representative strain rates, normalized by the value at 320 μm, generally scale with $1/\lambda$, as predicted by Eq. (3). For the larger $\eta_0 k$'s, they scale less strongly than expected because increasing strength somewhat suppresses the strain rate scaling.

sensitivity of the RMI estimates is sufficient to eliminate the possibility of strain hardening.

F. Scaling effectiveness

Figure 11 shows a check of the strain rate scaling with length scale. The representative strain rates from PRS are first normalized by the representative strain rate for the same $\eta_0 k$ and $\lambda = 320 \, \mu\mathrm{m}$ and then plotted vs $1/\lambda$. Thus, the curve for each $\eta_0 k$ starts at 1. A line shows the scaling expected based on Eq. (3). The representative strain rates are slightly suppressed below the scaling line because the strength increases with increasing strain rate (decreasing λ). That effect increases with increasing $\eta_0 k$ as perturbations become less stable and strength has more effect on the growth rates. The strength suppression of strain rate is not noticeable at $\eta_0 k = 0.3$, but at 0.9, the expected scaling factor for $\lambda = 65 \, \mu\mathrm{m}$ of 4.92 is reduced by 26% to 3.63. Note that a similar plot based on the location of the PRS dominant peak in Fig. 8 rather than the centroid gives a very similar result, indicating that the methodology for calculating the centroid is not providing a misleading result. Also, hydrocode simulations using the same strength value for all λ's matched the theoretical scaling, indicating that strength differences are what suppressed the scaling.

Figure 12 checks for scaling with $\eta_0 k$ from Eq. (3) now using absolute values, as compared with normalized, of the PRS centroid strain rates. Since we are using representative values rather than a specific location or time, f and g were replaced by a constant of 3.3 adjusted to fit the data. Scaling the strain rate by $\eta_0 k$ works well for the larger λ's but less so for $\lambda = 65 \, \mu\mathrm{m}$. Here, $\lambda = 65 \, \mu\mathrm{m}$ has the highest strength
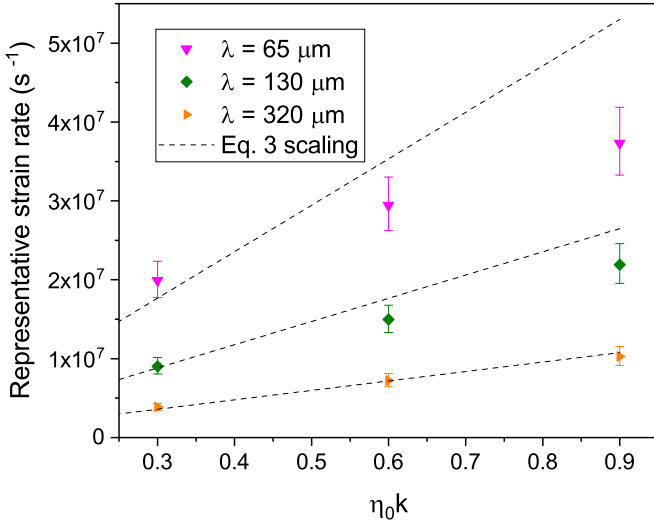
FIG. 12. Equation (3) predicts the scaling of experimental strain rates with $\eta_0 k$ at least well enough for experiment design.

values, and Eq. (3) tacitly assumes that the strength does not change when λ or $\eta_0 k$ changes, which is clearly not correct. Overall, especially considering that it is the log of the strain rate that is important, $\eta_0 k$ scaling from Eq. (3) would serve well at least for initial experiment design.

G. Scaling practical limits

Fielding the widest possible range of λ's on a target would give the best resolution of the change in strength with strain rate. It could also potentially allow overlap with other techniques, such as mini-Hopkinson bars [39], to independently validate the strength estimates. Distinct practical considerations limit both the maximum and minimum λ's.

The minimum λ is mostly constrained by machining limitations. Geometrically, fly cutting a given $\eta_0 k$ sine wave profile with a smaller λ requires a sharper (smaller tip radius) tool, which wears more quickly. Replacing a dull tool and indicating the new tool to an in-progress profile is always part of the machining process, but it becomes increasingly more burdensome when the tool radius decreases below some threshold depending on the hardness of the material, and the tool wears more quickly. Roughly speaking, machining limitations start to become a consideration when λ goes $< \sim 50\,\mu m$. PDV limitations on resolving spatial regions close to the wavelength of the laser light and on time resolving spike growth at faster strain rates also come into play for significantly smaller wavelengths.

Two factors limit the maximum λ. First, area is limited on the target. To isolate strain rate effects as in this paper, multiple regions with different λ's must fit on the same target to identical loading. The simulations to quantify the strength estimate assume an infinitely repeating series of perturbations. To ensure that the PDV measures only perturbations that match that assumption, each perturbation region must span the PDV spot size plus a couple more wavelengths on either side to avoid perturbations that have edge effects from the nearby

flat regions [24]. Thus, large λ's can quickly eat up available space.

Secondly, the 4 mm collimating PDV probes, the larger ones that gave good data, had a spot size of ~ 2 mm. To estimate strength, we must capture at least the spike velocity, and aligning a small laser spot to the perturbation trough is nontrivial due to the tolerances in the probe manufacturing and the laser wavelength being invisible to the human eye at 1550 nm. Without special alignment effort, ensuring that a spike is captured in the measurement spot limits the maximum perturbation wavelength to the spot size.

With the techniques used in this paper, increasing the λ range beyond about a factor of 10 would become increasingly challenging.

H. Grain scale effects

Our smallest λ of 65 μm is about the same as the grain size, and the initial perturbation amplitudes ($2\eta_0$) for that case range from 6.2 to 18.6 μm. One could ask if grain-scale heterogeneity might affect the measured velocity data. The issue of grain scale heterogeneity on measured velocities used for strength estimates has been studied by Zuanetti *et al.* [84], although only for the cases of planar impact and pressure-shear testing. For those, the loading is one-dimensional compared with the two-dimensional deformation state for RMI. Nonetheless, some of the observations are relevant. First and foremost, regardless of grain size effects, velocities measured at a point for any ensemble of repeated tests are expected to converge to the isotropic continuum mean. The scatter in such measurements, however, would increase for increasing grain size.

We do not measure velocity at a point. In the case of the 65-μm-wavelength perturbations, the number of grains along the length of all the spikes sampled within the PDV spot is large. For the smallest 2.7 mm probe with ~ 1.35 mm spot diameter on the target, there should be ~ 350 grains along the length of the sampled spike regions. The fewest grains sampled in this experiment would be ~ 70 grains in the spike length seen by that same probe for the 320 μm wavelength because there are fewer perturbations in the spot. Since that is still a significant sample, the dominant measured velocities should correspond more to an ensemble average than to a point measurement at one grain. Because it depends on the area of the spot, the 4 mm probe sees more than twice as many grains. Furthermore, the two nonoverlapping PDV spots for the 2.7 and 4 mm probes effectively serve like the multiple experiments of Zuanetti *et al.* [84] as far as at least representing one repeat experiment. If grain scale heterogeneity were significant, one could expect the different probes to disagree noticeably. In Fig. 6, the two probes on each region agree within uncertainty, indicating no heterogeneity effects within the resolution of these experiments.

V. CONCLUSIONS

For RMI experiments for solid strength, a straightforward theoretical analysis shows that the strain rate for a given shock load should be proportional to $\eta_0 k / \lambda$. A series of impact-driven RMI experiments in copper were

executed with different length scale (wavelength, λ) perturbations on single targets but with the same nondimensional amplitude $\eta_0 k$. This configuration largely isolates the effect of strain rate on strength. The estimated strengths increased by $\sim 70\%$ from 700 to 1200 MPa when λ decreased from 320 to 65 μm, a factor of 4.9. Experiments at three $\eta_0 k'$s exercised increasing amounts of plastic strain yet, since the strength estimate did not change, showed no evidence of strain hardening.

PRS simulations allowed an objective determination of the effective strain rate for each experiment, ranging from 8.7×10^6 s^{-1} for 320 μm λ perturbations to 3.3×10^7 s^{-1} for 65 μm λ perturbations. The strain rates were known very precisely relative to one another allowing an estimate of $dY/d(\log_{10} \dot{\varepsilon})$, the strain-rate-hardening slope, as 830 ± 160 MPa $\cdot \log_{10}$(s). Using the effective strain rates, the RMI strength estimates were plotted against constitutive testing data from the literature to show a striking resolution of the strength upturn at higher strain rates.

The theoretical strain rate scaling by $1/\lambda$ was mildly suppressed by the significant strength increase with strain rate, but the basic scaling objective was achieved.

[1] J. F. Barnes, P. J. Blewett, R. G. McQueen, K. A. Meyer, and D. Venable, Taylor instability in solids, J. Appl. Phys. **45**, 727 (1974).

[2] A. G. Ivanov, V. A. Ogorodnikov, G. Ya. Karpenko, A. D. Kovtun, A. A. Demidov, and L. A. Tolstikova, Effect of shear strength on the development of instability during the deceleration of imploding casings, J. Appl. Mech. Tech. Phys. **35**, 639 (1994).

[3] H.-S. Park, K. T. Lorenz, R. M. Cavallo, S. M. Pollaine, S. T. Prisbrey, R. E. Rudd, R. C. Becker, J. V. Bernier, and B. A. Remington, Viscous Rayleigh-Taylor instability experiments at high pressure and strain rate, Phys. Rev. Lett. **104**, 135504 (2010).

[4] Y. Zhou, R. J. R. Williams, P. Ramaprabhu, M. Groom, B. Thronber, A. Hillier, W. Mostert, B. Rollin, S. Balachandar, P. D. Powell *et al.*, Rayleigh-Taylor and Richtmyer-Meshkov instabilities: A journey through scales, Physica D **423**, 132838 (2021).

[5] K. O. Mikaelian, Richtmyer-Meshkov instability of arbitrary shapes, Phys. Fluids **17**, 034101 (2005).

[6] A. R. Piriz, J. J. López Cela, N. A. Tahir, and D. H. H. Hoffmann, Richtmyer-Meshkov instability in elastic-plastic media, Phys. Rev. E **78**, 056401 (2008).

[7] A. R. Piriz, J. J. López Cela, and N. A. Tahir, Richtmyer-Meshkov instability as a tool for evaluating material strength under extreme conditions, Nucl. Instrum. Methods. Phys. Res. A **606**, 139 (2009).

[8] G. Dimonte, G. Terrones, F. J. Cherne, T. C. Germann, V. Dupont, K. Kadau, W. T. Buttler, D. M. Oro, C. Morris, and D. L. Preston, Use of the Richtmyer-Meshkov instability to infer yield stress at high-energy densities, Phys. Rev. Lett. **107**, 264502 (2011).

[9] W. T. Buttler, D. M. Oró, D. L. Preston, K. O. Mikaelian, F. J. Cherne, R. S. Hixson, F. G. Mariam, C. Morris, J. B. Stone, G. Terrones *et al.*, Unstable Richtmyer-Meshkov growth of solid and liquid metals in vacuum, J. Fluid Mech. **703**, 60 (2012).

[10] K. K. John, Strength of tantalum at high pressures through Richtmyer-Meshkov laser compression experiments and simulations, Ph.D. thesis, California Institute of Technology, 2014.

[11] B. J. Jensen, F. J. Cherne, M. B. Prime, K. Fezzaa, A. J. Iverson, C. A. Carlson, J. D. Yeager, K. J. Ramos, D. E. Hooks, J. C. Cooley, and G. Dimonte, Jet formation in cerium metal to examine material strength, J. Appl. Phys. **118**, 195903 (2015).

[12] S. Opie, S. Gautam, E. Fortin, J. Lynch, P. Peralta, and E. Loomis, Behaviour of rippled shocks from ablatively-driven Richtmyer-Meshkov in metals Accounting for strength, J. Phys. Conf. Ser. **717**, 012075 (2016).

[13] Z. Sternberger, B. R. Maddox, Y. P. Opachich, C. E. Wehrenberg, R. G. Kraus, B. A. Remington, G. C. Randall, M. Farrell, and G. Ravichandran, A comparative study of Rayleigh-Taylor and Richtmyer-Meshkov instabilities in 2D and 3D in tantalum, AIP Conf. Proc. **1793**, 110006 (2017).

[14] M. S. Freeman, C. Rousculp, D. Oro, S. Kreher, B. Cheng, J. Griego, A. Patten, L. Neukirch, R. Reinovsky, P. Turchi *et al.*, The spikes from Richtmyer-Meshkov instabilities in pulsed power cylindrical experiments, AIP Conf. Proc. **1979**, 080005 (2018).

[15] M. Hudspeth, J. Olles, A. Mandal, J. Williams, S. Root, and T. Vogler, Strength of porous $\alpha - SiO_2$ in a shock loaded environment: Calibration via Richtmyer-Meshkov instability and validation via Mach lens, J. Appl. Phys. **128**, 205901 (2020).

[16] J. D. Olles, M. C. Hudspeth, C. F. Tilger, and T. J. Vogler, The effect of liquid tamping media on the growth of Richtmyer-Meshkov instability in copper, J. Dyn. Behav. Mater. **7**, 338 (2021).

[17] T. J. Vogler and M. C. Hudspeth, Tamped Richtmyer-Meshkov instability experiments to probe high-pressure material strength, J. Dyn. Behav. Mater. **7**, 262 (2021).

[18] J. A. Stewart, J. D. Olles, and M. A. Wood, Elucidating size effects on the yield strength of single-crystal Cu via the Richtmyer-Meshkov instability, J. Appl. Phys. **131**, 114901 (2022).

[19] S. Y. Grigoryev, S. A. Dyachkov, A. N. Parshikov, and V. V. Zhakhovsky, Limited and unlimited spike growth from grooved free surface of shocked solid, J. Appl. Phys. **131**, 065104 (2022).

[20] G. Whiteman, B. Adams, B. Thorington-Jones, and J. G. Turner, Richtmyer-Meshkov instability experiments on three body-centred cubic metals, AIP Conf. Proc. **2844**, 370007 (2023).

[21] M. B. Prime, W. T. Buttler, M. A. Buechler, N. A. Denissen, M. A. Kenamond, F. G. Mariam, J. I. Martinez, D. M. Oró, D. W. Schmidt, J. B. Stone *et al.*, Estimation of metal strength at very high rates using free-surface Richtmyer-Meshkov instabilities, J. Dyn. Behav. Mater. **3**, 189 (2017).

[22] M. B. Prime, A. Arsenlis, R. A. Austin, N. R. Barton, C. C. Battaile, J. L. Brown, L. Burakovsky, W. T. Buttler, S.-Ro. Chen, D. M. Dattelbaum *et al.*, A broad study of tantalum strength from ambient to extreme conditions, Acta Mater. **231**, 117875 (2022).

[23] J. L. Brown, M. B. Prime, N. R. Barton, D. J. Luscher, L. Burakovsky, and D. Orlikowski, Experimental evaluation of shear modulus scaling of dynamic strength at extreme pressures, J. Appl. Phys. **128**, 045901 (2020).

[24] M. B. Prime, W. T. Buttler, S. J. Fensin, D. R. Jones, J. L. Brown, R. S. King, R. Manzanares, D. T. Martinez, J. I. Martinez, J. R. Payton *et al.*, Tantalum strength at extreme strain rates from impact-driven Richtmyer-Meshkov instabilities, Phys. Rev. E **100**, 053002 (2019).

[25] A. Kumar and R. G. Kumble, Viscous drag on dislocations at high strain rates in copper, J. Appl. Phys. **40**, 3475 (1969).

[26] P. S. Follansbee, U. F. Kocks, and G. Regazzoni, The mechanical threshold of dynamically deformed copper and nitronic 40, J. Phys. Colloques **46**, C5-25 (1985).

[27] H. Couque, The use of the direct impact Hopkinson pressure bar technique to describe thermally activated and viscous regimes of metallic materials, Philos. Trans. R. Soc. A **372**, 20130218 (2014).

[28] J. L. Jordan, C. R. Siviour, G. Sunny, C. Bramlette, and J. E. Spowart, Strain rate-dependant mechanical properties of OFHC Copper, J. Mater. Sci. **48**, 7134 (2013).

[29] E. Avriel, Z. Lovinger, R. Nemirovsky, and D. Rittel, Investigating the strength of materials at very high strain rates using electro-magnetically driven expanding cylinders, Mech. Mater. **117**, 165 (2018).

[30] W. Tong, R. J. Clifton, and S. Huang, Pressure-shear impact investigation of strain rate history effects in oxygen-free high-conductivity copper, J. Mech. Phys. Solids **40**, 1251 (1992).

[31] S. Nemat-Nasser and Y. Li, Flow stress of f.c.c. polycrystals with application to OFHC Cu, Acta Mater. **46**, 565 (1998).

[32] Z. Rosenberg, R. Kositski, and A. Malka-Markovitz, The effective strength of metallic plates perforated by rigid projectiles, Int. J. Impact Eng. **121**, 35 (2018).

[33] M. A. Meyers, U. R. Andrade, and A. H. Chokshi, The effect of grain size on the high-strain, high-strain-rate behavior of copper, Metall. Mater. Trans. A **26**, 2881 (1995).

[34] D. Ostwaldt and P. Klimanek, The influence of temperature and strain rate on microstructural evolution of polycrystalline copper, Mater. Sci. Eng. A **234**, 810 (1997).

[35] Z. Rosenberg, Y. Ashuach, V. Leus, and A. Malka-Markovitz, On the upturn phenomenon in the strength vs. strain-rate relations of metals, Int. J. Solids Struct. **176–177**, 185 (2019).

[36] T. J. Vogler, On measuring the strength of metals at ultrahigh strain rates, J. Appl. Phys. **106**, 053530 (2009).

[37] D. T. Casem, S. E. Grunschel, and B. E. Schuster, Normal and transverse displacement interferometers applied to small diameter Kolsky bars, Exp. Mech. **52**, 173 (2012).

[38] D. A. Gorham, P. H. Pope, and J. E. Field, An improved method for compressive stress-strain measurements at very high strain rates, Proc. R. Soc. Lond. A **438**, 153 (1992).

[39] D. Casem, 6—Miniature Kolsky bar methods, Adv. Exp. Impact Mech. 149 (2022).

[40] G. Whiteman, L. J. Lea, R. M. Quinn, M. J. Cox, P. A. Hooper, and D. M. Williamson, High strain-rate characterisation of vanadium, J. Dyn. Behav. Mater. **9**, 315 (2023).

[41] L. J. Lea and A. P. Jardine, Characterisation of high rate plasticity in the uniaxial deformation of high purity copper at elevated temperatures, Int. J. Plast. **102**, 41 (2018).

[42] R. D. Richtmyer, Taylor instability in shock acceleration of compressible fluids, Commun. Pure Appl. Math. **13**, 297 (1960).

[43] K. A. Meyer and P. J. Blewett, Numerical investigation of the stability of a shock-accelerated interface between two fluids, Phys. Fluids **15**, 753 (1972).

[44] G. Dimonte, G. Terrones, F. J. Cherne, and P. Ramaprabhu, Ejecta source model based on the nonlinear Richtmyer-Meshkov instability, J. Appl. Phys. **113**, 024905 (2013).

[45] This comes from substituting Eqs. 2.9 and 2.21 in Buttler et al. [9] into Eq. 2.17. The $f(x, y)$ in Eq. 2.17 is in error [W. T. Buttler (private communication)], but does not change the scaling relation.

[46] S. J. Fensin, E. K. Walker, E. K. Cerreta, C. P. Trujillo, D. T. Martinez, and G. T. Gray III, Dynamic failure in two-phase materials, J. Appl. Phys. **118**, 235305 (2015).

[47] O. T. Strand, D. R. Goosman, C. Martinez, T. L. Whitworth, and W. W. Kuhlow, Compact system for high-speed velocimetry using heterodyne techniques, Rev. Sci. Instrum. **77**, 083108 (2006).

[48] D. N. Blaschke, T. Nguyen, M. Nitol, D. O'Malley, and S. Fensin, Machine learning based approach to predict ductile damage model parameters for polycrystalline metals, Comput. Mater. Sci. **229**, 112382 (2023).

[49] E. J. Caramana, D. E. Burton, M. J. Shashkov, and P. P. Whalen, The construction of compatible hydrodynamics algorithms utilizing conservation of total energy, J. Comput. Phys. **146**, 227 (1998).

[50] D. E. Burton, T. C. Carney, N. R. Morgan, S. R. Runnels, S. K. Sambasivan, and M. J. Shashkov, A Cell-Centered Lagrangian Hydrodynamics Method for Multi-Dimensional Unstructured Grids in Curvilinear Coordinates with Solid Constitutive Models, Technical Report No. LA-UR-11-04995 (Los Alamos National Laboratory, Los Alamos, 2011).

[51] M. Kenamond, M. Bement, and M. Shashkov, Compatible, total energy conserving and symmetry preserving arbitrary Lagrangian-Eulerian hydrodynamics in 2D $Rz-$Cylindrical coordinates, J. Comput. Phys. **268**, 154 (2014).

[52] D. E. Burton, Connectivity structures and differencing techniques for staggered-grid free-Lagrange hydrodynamics, in *Seventh IMACS International Conference on Computer Methods for Partial Differential Equations* (New Brunswick, NJ, 1992).

[53] D. E. Burton, Consistent Finite-Volume Discretization of Hydrodynamic Conservation Laws for Unstructured Grids, Report

UCRL–JC–118788 (Lawrence Livermore National Laboratory, Livermore, 1994).

[54] J. VonNeumann and R. D. Richtmyer, A method for the numerical calculation of hydrodynamic shocks, J. Appl. Phys. **21**, 232 (1950).

[55] C. W. Greeff, S. D. Crockett, L. Burakovsky, and S. P. Rudin, Limited Range Sesame EOS for Ta, Technical Report LA-UR-17-22600 (Los Alamos National Laboratory, Los Alamos, 2017), https://doi.org/10.2172/1351253.

[56] D. L. Preston, D. L. Tonks, and D. C. Wallace, Model of plastic deformation for extreme loading conditions, J. Appl. Phys. **93**, 211 (2003).

[57] J. H. Peterson, K. G. Honnell, C. Greeff, J. D. Johnson, J. Boettger equation of state for copper, AIP Conf. Proc. **1426**, 763 (2012).

[58] L. Burakovsky, C. W. Greeff, and D. L. Preston, Analytic model of the shear modulus at all temperatures and densities, Phys. Rev. B **67**, 094107 (2003).

[59] T. Ao and D. Dolan, SIRHEN: A data reduction program for photonic Doppler velocimetry measurements, in Technical Report SAND2010-3628 (Sandia National Laboratories, Albuquerque, 2010), https://doi.org/10.2172/989357.

[60] C. R. Lear, D. R. Jones, M. B. Prime, and S. J. Fensin, SAVER: A peak velocity extraction program for advanced photonic Doppler velocimetry analysis, J. Dyn. Behav. Mater. **7**, 510 (2021).

[61] M. B. Prime, J. S. Merson, and S. R. Chen, Physical regime sensitivity, J. Dyn. Behav. Mater. **9**, 248 (2023).

[62] J. W. Dyer, J. Waters, and M. B. Prime, Robust implementation of physical regime sensitivity and demonstration on Richtmyer-Meshkov instability experiments, 23rd Biennial Conference of the APS Topical Group on Shock Compression of Condensed Matter (2023).

[63] A. R. Piriz, J. J. López Cela, S. A. Piriz, and N. A. Tahir, Two-dimensional simulations of Rayleigh-Taylor instability in elastic-plastic media, Phys. Rev. E **108**, 055102 (2023).

[64] See Supplemental Material at http://link.aps.org/supplemental/10.1103/PhysRevE.109.015002 for details and results on the extraction of maximum spike velocities as well as raw oscilloscope data for all the probes.

[65] C. R. Lear, M. R. Chancey, R. Flanagan, J. G. Gigax, M. T. Hoang, D. R. Jones, H. Kim, D. T. Martinez, B. M. Morrow, N. Mathew *et al.*, Transition in helium bubble strengthening of copper from quasi-static to dynamic deformation, Acta Mater. **254**, 118987 (2023).

[66] B. W. Reed, J. R. Patterson, J. H. Nguyen, J. S. Stölken, and M. Kumar, Bounds on the rate-dependent plastic flow of tantalum up to 75 GPa, J. Dyn. Behav. Mater. **7**, 307 (2021).

[67] P. S. Follansbee and G. T. Gray, Dynamic deformation of shock prestrained copper, Mater. Sci. Eng. A **138**, 23 (1991).

[68] G. T. Gray and K. S. Vecchio, Influence of peak pressure and temperature on the structure/property response of shock-loaded Ta and Ta-10W, Metall. Mater. Trans. A **26**, 2555 (1995).

[69] M. A. Meyers, *Dynamic Behavior of Materials* (John Wiley & Sons, New York, 1994).

[70] A. Rohatgi, K. S. Vecchio, and I. G. T. Gray, A metallographic and quantitative analysis of the influence of stacking fault energy on shock-hardening in Cu and Cu–Al alloys, Acta Mater. **49**, 427 (2001).

[71] J. D. Olles, M. Hudspeth, C. F. Tilger, C. Garasi, N. Sanchez, and B. Jensen, Hydrodynamic Richtmyer-Meshkov instability of metallic solids used to assess material deformation at high strain-rates, in *Dynamic Behavior of Materials*, Vol. 1. Conference Proceedings of the Society for Experimental Mechanics Series, edited by L. Lamberson (Springer International Publishing, Cham, 2020), p. 149.

[72] H. Chawla, S. Yadav, H. Aprahamian, and D. Sagapuram, Determining large-strain metal plasticity parameters using *in situ* measurements of plastic flow past a wedge, Proc. R. Soc. A **479**, 20230061 (2023).

[73] Z. Sternberger, Y. Opachich, C. Wehrenberg, R. Kraus, B. Remington, N. Alexander, G. Randall, M. Farrell, and G. Ravichandran, Investigation of hydrodynamic instability growth in copper, Int. J. Mech. Sci. **149**, 475 (2018).

[74] S. Ravindran, V. Gandhi, Z. Lovinger, M. Mello, and G. Ravichandran, Dynamic strength of copper at high pressures using pressure shear plate experiments, J. Dyn. Behav. Mater. **7**, 248 (2021).

[75] R. J. Edwards, S. D. Rothman, T. J. Vogler, and M. D. Furnish, Inferring the high-pressure strength of copper by measurement of longitudinal sound speed in a symmetric impact and release experiment, J. Appl. Phys. **125**, 145901 (2019).

[76] L. C. Chhabildas and J. R. Asay, Time-resolved wave profile measurements in copper to Megabar pressures, Conference: 8. AIRAPT Conference and 19. EHPRG Conference, Uppsala, Sweden (U.S. Department of Energy, 1981).

[77] J. C. F. Millett, N. K. Bourne, and Z. Rosenberg, Shear stress measurements in copper, iron, and mild steel under shock loading conditions, J. Appl. Phys. **81**, 2579 (1997).

[78] D. McGonegle, A. Higginbotham, E. Galtier, E. E. McBride, M. I. McMahon, D. Milathianaki, H. J. Lee, B. Nagler, S. M. Vinko, and J. S. Wark, Investigations into rapid uniaxial compression of polycrystalline targets using femtosecond x-ray diffraction, J. Phys. Conf. Ser. **500**, 112063 (2014).

[79] J. L. Brown, J. P. Davis, and C. T. Seagle, Multi-megabar dynamic strength measurements of Ta, Au, Pt, and Ir, J. Dyn. Behav. Mater. **7**, 196 (2021).

[80] B. A. Remington, H.-S. Park, D. T. Casey, R. M. Cavallo, D. S. Clark, C. M. Huntington, D. H. Kalantar, C. C. Kuranz, A. R. Miles, S. R. Nagel *et al.*, Rayleigh-Taylor instabilities in high-energy density settings on the National Ignition Facility, Proc. Natl. Acad. Sci. U.S.A. **116**, 18233 (2019).

[81] L. J. Lea and S. M. Walley, High strain rate metal plasticity, in *Encyclopedia of Continuum Mechanics*, edited by H. Altenbach and A. Öchsner (Springer, Berlin, Heidelberg, 2020), p. 1072.

[82] L. Lea, L. Brown, and A. Jardine, Time limited self-organised criticality in the high rate deformation of face centred cubic metals, Commun. Mater. **1**, 93 (2020).

[83] P. Bak, *How Nature Works: The Science of Self-Organized Criticality* (Springer Science & Business Media, New York, 2013).

[84] B. Zuanetti, D. J. Luscher, K. Ramos, and C. Bolme, Unraveling the implications of finite specimen size on the interpretation of dynamic experiments for polycrystalline aluminum through direct numerical simulations, Int. J. Plast. **145**, 103080 (2021).